LED-Switchable High-Q Packaged THz Microbeam Resonators

Stephen M. Hanham, *Member, IEEE*, Munir M. Ahmad, Stepan Lucyszyn, *Fellow, IEEE*, and Norbert Klein

Abstract—This paper describes the design, fabrication, and experimental characterization of photonic crystal microbeam cavity resonators for the terahertz band implemented using suspended dielectric rectangular waveguide (DRW) in high-resistivity silicon. Electrical quality factors of up to 11 900, combined with small modal volumes of 0.28 and 0.077 mm^3, are demonstrated for devices operating at 100 and 200 GHz, respectively. The devices are found to be extremely light-sensitive, opening up new opportunities for light-controlled switching devices at terahertz frequencies. It is shown that the quality factor of the resonator can be tuned and the resonance extinguished through photo-illumination with an infrared light-emitting diode (IR LED). Additionally, the questions of thermal tunability and thermal stability of the resonators are examined. The demonstrated resonators are inherently suited to integration with DRW and, by silicon bulk micromachining, represent an attractive approach for realizing microphotonic-integrated circuits for terahertz systems-on-a-substrate.

Index Terms—Optical resonators, photonic crystals, photonic-integrated circuits, submillimeter-wave integrated circuits.

I. INTRODUCTION

HIGH quality (Q-) factor resonators form the basis of millimeter and submillimeter wave system components, such as low phase-noise oscillators, impedance matching networks, and narrowband filters [1]. They can also serve as sensing platforms by enhancing light–matter interaction, allowing for highly sensitive dielectric measurements and chemical sensing [2], [3]. The system integration of these resonators will be critical to realizing advanced terahertz systems.

Recently, suspended dielectric rectangular waveguide (DRW) fabricated from high resistivity silicon (HRS) has emerged as a promising waveguide technology for integrated terahertz circuits, exhibiting very low loss across the terahertz frequency band [4], [5]. In this work, the application of this technology toward the creation of inline waveguide resonators and filters

that are suitable for terahertz systems-on-a-substrate is demonstrated.

An electromagnetic (or photonic) bandgap can be induced in a DRW for transverse electric (TE) and transverse magnetic (TM) modes through the introduction of a linear array of cylindrical air holes through the DRW (array axis in the waveguide direction) [6], [7]. By careful tuning of hole radii and positions, it is possible to create a localized state within the waveguide bandgap that supports a high Q-factor resonance, which can be coupled to by the fundamental TE or TM DRW mode [7].

This approach to creating high-Q resonators from one-dimensional (1-D) photonic crystal cavities in DRW has been successfully demonstrated at infrared (IR) and optical wavelengths, for silicon-on-insulator (SOI) [8]–[10] and free-standing nanobeam [11]–[15] structures, achieving theoretical Q-factors as high as 5×10^9 [15]. 1-D photonic crystal resonators (PCRs) have several significant advantages over the more common photonic crystal slab [two-dimensional (2-D) periodicity] resonators:

1) inherently suited for DRW integration and more amendable to photonic-integrated circuits;
2) easier to design and occupy less silicon real estate; and
3) can realize smaller modal volumes (V) [11], [12] leading to higher Purcell factors [16] (modification of the spontaneous emission of a quantum emitter by its environment [17], [18]).

In this paper, we describe the use of suspended HRS DRW to form microbeam PCRs (MPCRs) and demonstrate the suitability of the technology for the millimeter-wave and terahertz bands by fabricating two MPCRs operating at 100 and 200 GHz. Furthermore, we show how these devices can be conveniently coupled to metal-pipe rectangular waveguide and packaged. In Section V, we investigate the light sensitivity of the devices and demonstrate how they can be switched using an inexpensive light source. In Section VI, the thermal tuning of the MPCRs is studied and the question of thermal stability for oscillator applications is addressed.

II. DESIGN OF MICROBEAM RESONATORS

The MPCR devices are formed by the through-wafer etching of a silicon wafer to produce single connected structures. The devices are composed of a central microbeam that is attached by ten narrow support beams to two outer regions of silicon, which function as supporting mounts, as shown in Fig. 1(a). The MPCR is mounted in a plastic shell, such that the microbeam
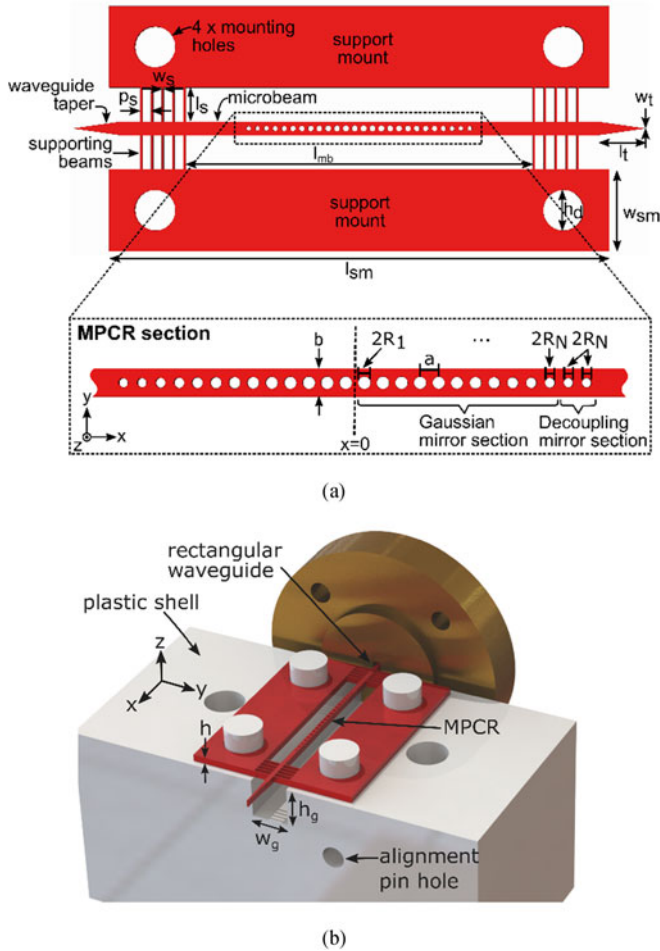
Fig. 1. (a) General design of the MPCR, consisting of a supported central silicon microbeam with waveguide tapers at either end. Holes in the microbeam create a 1-D photonic crystal cavity that supports several resonant modes. (b) Illustration showing how the MPCRs are suspended over a channel in the 3-D printed packaging to form a low-loss terahertz waveguide and high Q-factor resonator. Note that the upper-half of the packaging, which sits on top of the etched silicon, has been removed for clarity.

Fig. 2. TE-mode band diagram for a unit cell consisting of a section of the silicon microbeam of width $b = 350$ μm, height $h = 525$ μm, and hole period $a = 450$ μm with an air hole of radius $R_i = 150$ μm. A band gap exists between the first and second TE modes, which is used to create the MPCR.

is suspended over a groove in the shell, as illustrated in Fig. 1(b), to avoid dielectric loss in the plastic. By suspending the microbeam, the loss in the DRW sections can be as low as 0.087 dB/cm at 100 GHz [4].

The ends of the microbeam feature a tapered section, which is used to form metal-pipe rectangular waveguide-to-DRW transitions by partial insertion of the microbeam-tapered ends into the aperture of a metal-pipe rectangular waveguide flange. The tapered section transitions from the microbeam width of b to a finishing width of w_t over a length l_t. The 100-GHz device has a linear taper and the 200-GHz device features an exponential taper ($y \propto e^{-0.86x}$), which gave improved insertion loss performance at the higher frequency.

A 1-D PCR is created in the middle of the microbeam through the introduction of a periodic linear array of air holes in the direction of the waveguide. Resonant electromagnetic modes are confined to the microbeam by total internal reflections at the silicon–air interfaces in the y- and z-directions and by
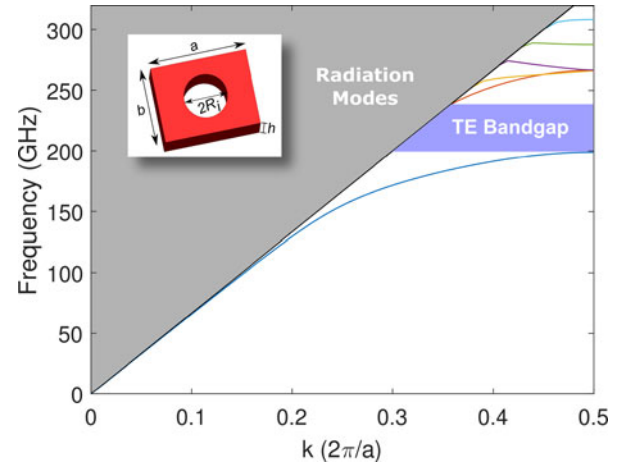
Bragg reflection by the holes in the direction of the waveguide (x-direction).

One of the key observations in the design of 1-D and 2-D PCRs is that in order to realize high Q-factor resonances with small modal volumes, the field distribution of the resonant mode must be shaped to reduce radiative losses [19]. This field-shaping is necessary to reduce the plane-wave components of the resonant mode that do not satisfy the condition for total internal reflections and, therefore, leak energy out of the microbeam. In the case of our MPCR, this corresponds to plane-waves with tangential component of the wavevector $\boldsymbol{k}_\parallel$ that fulfill the inequality $0 \leq \boldsymbol{k}_\parallel \leq 2\pi/\lambda_0$ in the x–z and x–y planes, where λ_0 is the free-space wavelength. The simplest approach to achieving this is to engineer the electric field profile of the resonant mode to be Gaussian [19].

The fine-tuning of the hole radii and positions to achieve a Gaussian modal profile can be a time-consuming numerical process. Fortunately, there are several design methodologies described in the literature [9], [15], [20] to simplify this process. We have found the design recipe given by Quan et al. [15], [20] to produce reliable results and this is the approach adopted in this paper.

The MPCR is assumed to be formed from $2N$ concatenated unit cells consisting of a section of the silicon microbeam of length a, width b, height h, and with an air hole of variable radius R_i, as shown in the inset of Fig. 2. The MPCR is symmetric about the y-axis and the design process reduces to the problem of determining the hole radii profile $\{R_1, R_2, \ldots, R_N\}$, once the microbeam dimensions are determined.

Quan et al. demonstrated that a high Q-factor nanobeam PCR can be obtained by arranging the unit cells to form two Bragg mirror sections that exhibit Gaussian attenuation of the field back-to-back. The required Gaussian field attenuation can be realized by making the mirror strength of each unit cell linearly increasing from the center to the outermost. Quan and Loncar

showed [15] that this is achieved when the unit cell filling fraction, defined as the ratio of the air hole area to the area of the microbeam unit cell ($f_i = \pi R_i^2/ab$), is tapered quadratically from a starting filling fraction f_{start} to a finishing filling fraction f_{end}. The simplest method for realizing this is an appropriate gradual reduction in the unit cell hole radius from the center unit cell to the outermost.

The design process begins by choosing a microbeam width b, hole period a, and air hole radius R_1 that leads to a bandgap with the band-edge of the lowest order dielectric mode approximately equal to the desired resonant frequency ω_{res}. Additionally, the dimension b is chosen to ensure a reasonably confined mode that is far from the light line with a high effective modal permittivity ϵ_{eff}. These dimensions determine the starting filling fraction f_{start}. The microbeam height h is determined by the thickness of the silicon wafer, conveniently chosen to be 525 μm.

Fig. 2 shows the TE modes band diagram for the case of the 200-GHz MPCR with microbeam width $b = 350$ μm, hole period $a = 450$ μm, and hole radius $R_i = 150$ μm. It can be seen from the diagram that a bandgap exists for modes with a TE symmetry between the lowest order dielectric mode and the next higher order mode; this is used for confining the resonance. A similar band diagram exists for the 100-GHz MPCR with the chosen dimensions $a = 650$ μm, $b = 1$ mm, and $R_i = 244$ μm. The band diagram was calculated using the software package MIT Photonics Band, which calculates the eigenmodes of Maxwell's equations for periodic structures by conjugate-gradient minimization of the block Rayleigh quotient on a plane-wave basis [21].

It can be shown from the band diagram calculations that the tapering of the unit cell hole radii, while maintaining a constant unit cell period, lowers the frequency of the band-edge of the first dielectric mode in the band diagram. This has the effect of increasing the mirror strength at the resonant frequency. The final hole radius R_N is chosen by selecting a final filling fraction f_{end} that maximizes the mirror strength [20]:

$$\gamma = \sqrt{\frac{(\omega_2 - \omega_1)^2}{(\omega_2 + \omega_1)^2} - \frac{(\omega_{\mathrm{res}} - \omega_0)^2}{\omega_0^2}} \qquad (1)$$

where ω_1 and ω_2 are the frequencies of the mode below and above the bandgap, respectively, and ω_0 is the mid-gap frequency. This is performed by sweeping the hole radius and calculating the band diagram and mirror strength for each case. A final hole radius of 190 and 84 μm was chosen for the 100- and 200-GHz devices, respectively.

The loaded *Q*-factor Q_l for a dielectric resonator can be expressed in terms of a sum of the reciprocals of its *Q*-factor contributions [1]

$$\frac{1}{Q_l} = \frac{1}{Q_d} + \frac{1}{Q_{\mathrm{rad}}} + \frac{1}{Q_{\mathrm{wg}}} \qquad (2)$$

where Q_d, Q_{rad}, and Q_{wg} are the *Q*-factors that characterize the loss due to the dielectric material, radiation, and the waveguide coupling, respectively [1]. By appropriate design of
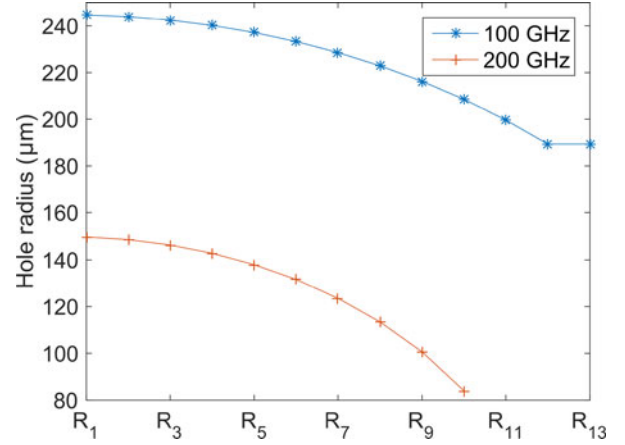

Fig. 3. Radii distribution of the air holes in the silicon microbeam for the two fabricated MPCRs.

the resonator, the radiation and waveguide loss terms in (2) can be made very small. This has been demonstrated in the IR band, where a similar design process realized a nanobeam PCR with a *Q*-factor of 5×10^9, limited by radiative losses [15]. In the terahertz band, the paucity of ultralow loss dielectric materials means that the *Q*-factor of a PCR is often limited by the loss tangent ($\tan\delta$) of the material, leading to [1]

$$Q_l \approx Q_d = 1/(\rho \tan\delta) \qquad (3)$$

where ρ is the dielectric filling factor describing the proportion of electric energy stored inside the dielectric relative to the total stored electric energy.

To achieve a material-loss limited *Q*-factor, the number of units cells forming the Bragg mirror is chosen to be sufficiently large that $Q_{\mathrm{rad}} \gg Q_d$ in (2). With our design, *N* was chosen to be 12 and 10 for the 100- and 200-GHz devices, respectively.

A final step is to control the coupling strength κ between the microbeam waveguide and the resonant mode to ensure that $Q_{\mathrm{wg}} \gg Q_d$ in (2). Full-wave electromagnetic simulations of the MPCR were performed using the finite-element method (FEM) solver in CST Microwave Studio to determine the coupling strengths. In the case of the 100-GHz MPCR, it was decided to introduce an additional unit cell, to the outside of the Bragg mirror section, with a hole radius equal to that which gives the greatest mirror strength to weaken the coupling. This is preferable to increasing *N*, which would have increased the modal volume. The 200-GHz design was left unmodified to maximize the strength of the signal to be measured at the higher operating frequency. Fig. 3 shows the hole radii distribution for the two devices.

To ensure that the field of the resonant mode was unaffected by nearby structures and to maximize *Q*-factor, several design decisions were made. The silicon either side of the microbeam was significantly cut-away to ensure that the gap between the microbeam and the supporting mount was larger than the modal field limits. Similarly, the plastic shell holding the MPCR was designed with a groove (depth h_g and width w_g) larger than the field limits, so that the field is isolated from the plastic

TABLE I
SUMMARY OF THE TWO DEVICES' GEOMETRICAL PARAMETERS

| Symbol	Quantity	100-GHz	200-GHz
N	Number of holes forming one Bragg mirror section	13	10
a	Hole period	650 μm	450 μm
b	Microbeam width	1000 μm	350 μm
h	Microbeam height	525 μm	525 μm
w_s	Support beam width	130 μm	70 μm
l_s	Support beam length	2500 μm	1250 μm
p_s	Support beam period	800 μm	400 μm
l_t	Taper length	3500 μm	3000 μm
w_t	Taper end width	0 μm	110 μm
-	Taper shape	Linear	Exponential
l_{mb}	Length of microbeam	25 540 μm	12 670 μm
w_{sm}	Width of support mount	6000 μm	5000 μm
l_{sm}	Length of support mount	36 700 μm	16 000 μm
h_g	Height of groove in shell	5000 μm	3000 μm
w_g	Width of groove in shell	6000 μm	2850 μm
h_d	Mounting hole diameter	3000 μm	3000 μm
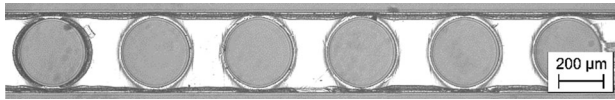
Fig. 4. Center six holes of the 200-GHz MPCR.

preventing further material losses. The width w_s and length l_s of the support beams were chosen to minimize leakage of energy away from the microbeam, based on the scaled results of [5], and were positioned away from the active region of the MPCR. The dimensions for the 100- and 200-GHz devices are summarized in Table I.

III. DEVICE FABRICATION

A. Silicon Deep Reactive Ion Etching

The MPCR devices were bulk-micromachined from a single silicon wafer, using a process adapted from the fabrication of microelectromechanical systems devices [22]. We utilize the Bosch process for the deep reactive-ion etching (DRIE) of the wafer, which is capable of fabricating high aspect ratio structures with nearly vertical sidewalls by cycling between plasma etching with SF_6 and deposition of a passivation layer with C_4F_8 [23]. This fabrication process has previously been described in detail [24] and is briefly summarized here.

A 525 $\pm$ 25 μm thick silicon wafer, with bulk resistivity greater than 10 kΩ·cm, is used to minimize free-carrier losses in the silicon. A 10 μm thick layer of photoresist (AZ9260), which is patterned using standard photolithographic techniques, is used as a soft mask for DRIE. The vertical etch rate of the DRIE process is dependent upon the aspect ratio of the features to be etched [23]. To achieve a consistent etch rate across the device, the mask was patterned with a 100 μm "halo" geometry, such that all etching occurs in trenches with a constant 100 μm width and the unwanted silicon areas "drop out" (see [23] for more details). Fig. 4 shows the center six holes of the 200-GHz MPCR exhibiting good circularity.
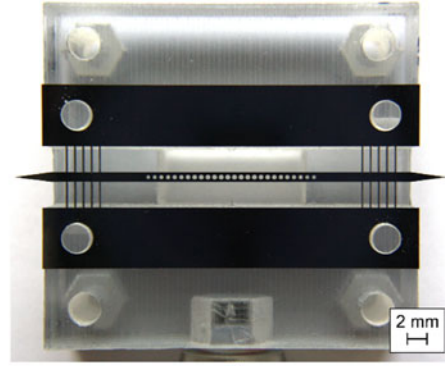
(a)
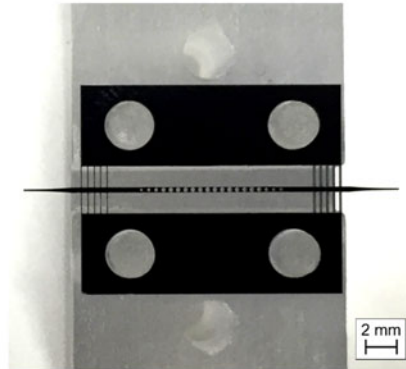
(b)
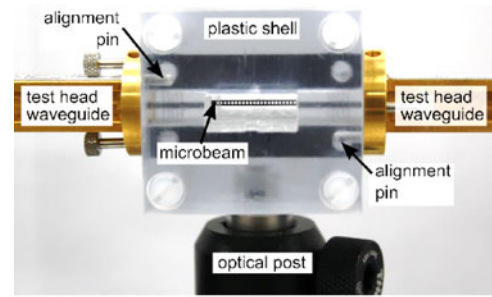
(c)

Fig. 5. Fabricated (a) 100-GHz and (b) 200-GHz MPCRs mounted in one half of their plastic shells. (c) 100-GHz MPCR fully mounted in its shell, supported between the waveguide flanges of the test heads of the VNA.

B. 3-D Printed Shell

The MPCR devices are packaged in a plastic shell that was 3-D-printed using a Stratasys Objet30 Pro printer. The shell was designed with a split-block construction, where the silicon MPCR is supported between the two halves of the shell. One of the shell halves has four printed alignment dowel pins that pass through the four mounting holes of the MPCR and into alignment holes on the other shell half, ensuring the accurate positioning of the three components. Fig. 5(a) and (b) shows the 100- and 200-GHz MPCR devices, respectively, mounted in the bottom half of their shells.

The shell includes holes on the end faces for the insertion of the alignment dowel pins belonging to the vector network analyzer (VNA) test head waveguide's UG-387 flange. This ensures that, when connected, the tapered section of the microbeam is
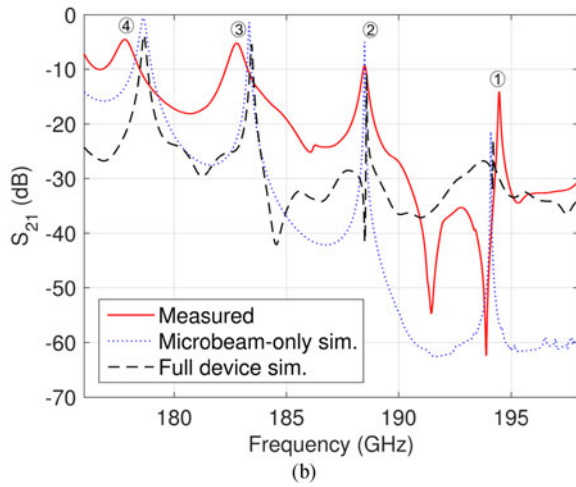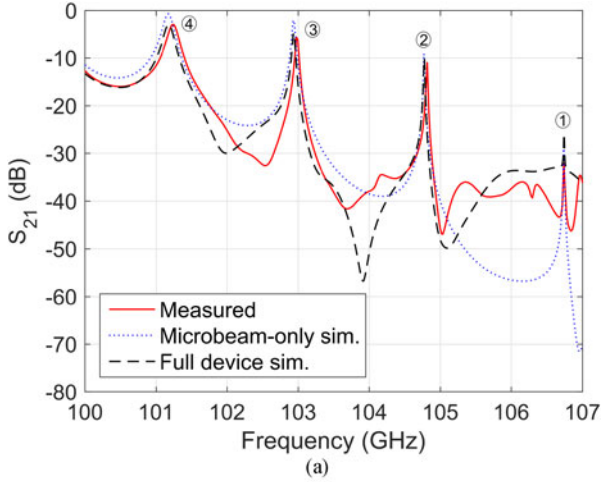
Fig. 6. Simulated and measured transmission responses for the (a) 100-GHz and (b) 200-GHz MPCRs.
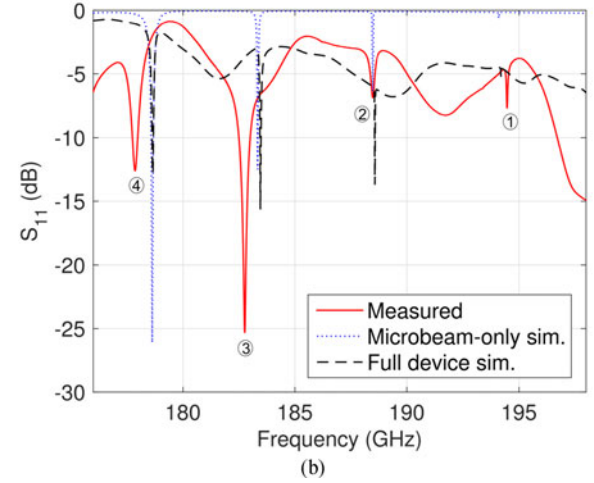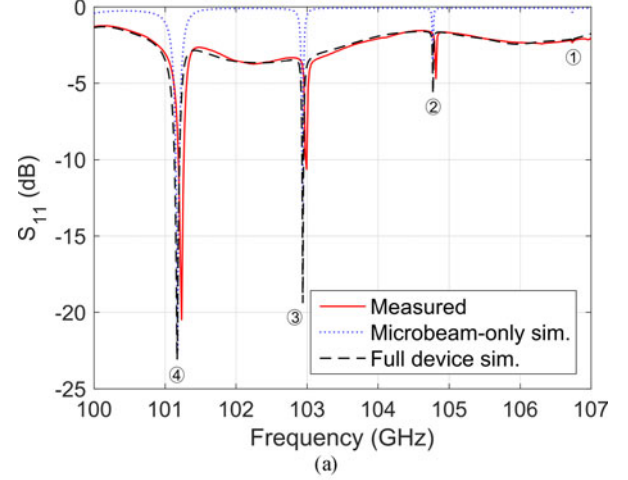

Fig. 7. Simulated and measured reflection responses for the (a) 100-GHz and (b) 200-GHz MPCRs.

centered inside the test head's rectangular waveguide, ensuring a reliable mechanical and electromagnetic interface. The shell is held together using nylon M3 screws and mounted on an optical post, as shown in Fig. 5(c).

IV. RESULTS AND DISCUSSION

The measurement of the scattering (*S*-) parameters for the two devices was carried out using a Rohde and Schwarz ZVA67, with the ZVA-Z110 (75–110 GHz, WR10) and ZVA-Z220 (140–220 GHz, WR5.1) millimeter-wave test heads. The thru-reflect-line technique was used to calibrate the instrument and define measurement reference planes at the test head waveguide UG-387 flanges.

Full-wave electromagnetic simulations of the devices were performed using the FEM solver in CST Microwave Studio. For the simulations, the real part of the relative permittivity of silicon is assumed to be $\epsilon'_r = 11.66$ [25]. The reported values for the loss tangent of HRS in this frequency range vary [25] and here the values $\tan \delta = 10^{-4}$ at 100 GHz and $\tan \delta = 0.5 \times 10^{-4}$ at 200 GHz are used.

Figs. 6 and 7 show the measured and simulated *S*-parameters for the 100- and 200-GHz devices. Four peaks are clearly visible in the forward voltage-wave transmission coefficient S_{21} frequency responses for both devices, corresponding to the four highest order resonant modes, numbered from high to low frequency. Fig. 8 shows the *y*-component of the electric field distribution (E_y) for these modes for the 200-GHz MPCR; the 100-GHz device has similar modal field distributions. Modes 1 and 3 have even distributions of E_y, while modes 2 and 4 are odd.

Two different simulated curves are shown in Figs. 6 and 7; one for the microbeam only and one for the full device, which includes the additional supporting beams, tapers, packaging, and test head waveguide flanges. Comparing the two curves, it can be seen that the tapers and supporting beams introduce additional loss, particularly notable in the input voltage-wave reflection coefficient S_{11} frequency responses for the 200-GHz device. Further simulations reveal that this is due to energy being coupled out of the microbeam by the supporting struts. This also has the effect of increasing the background S_{21}, leading to an increase in the level of the troughs between resonance peaks.
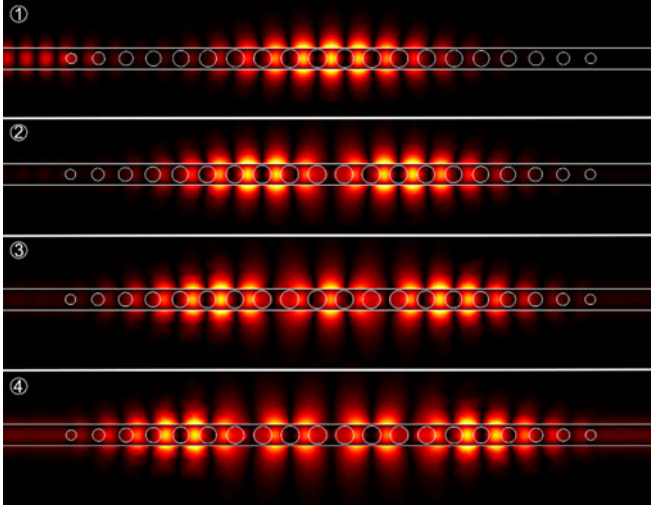
Fig. 8. Simulated electric field $|E_y|$ for the four resonant modes of the 200-GHz MPCR, shown from lowest (top) to highest (bottom) order. The 100-GHz MPCR has similar modal field distributions.

It is recommended that with future devices, the supporting struts be made narrower and their period further optimized to reduce this effect.

There is a small offset of the resonant frequency of the four resonant modes between the simulated and measured curves, particularly evident for the 200-GHz device. It is thought that this is caused by two factors. First, the microbeam holes were slightly over-etched leading to larger radii than designed. Second, the thickness of the silicon wafer used for fabrication has a thickness tolerance of ± 25 μm. Simulations of the 200-GHz device show that this can lead to a shift of the resonant frequencies of the four peaks by up to 2 GHz accompanied by a small reduction in Q-factor.

A. Resonance Quality Factor

For high values, the loaded Q-factor of the MPCR's resonant modes can be calculated from the measured S_{21} results, using the full-width at half-maximum (FWHM) frequency bandwidth Δf of the resonant peaks around a center frequency f_0 by [1]

$$Q_l = \frac{f_0}{\Delta f}. \qquad (4)$$

The FWHM of the resonant peaks is estimated by fitting a Lorentzian curve to $|S_{21}|^2$ over a frequency range corresponding to the amplitude being within 5 dB of the peak level. All fits exhibited a coefficient of determination better than 0.99. Table II summarizes the Q-factors calculated using this method with the stated uncertainties determined from the amplitude inaccuracy of the VNA as described in [26]. It can be seen that the fundamental resonance mode of the 100-GHz MPCR achieves a very high Q-factor of $11\,900 \pm 500$. The 200-GHz MPCR has a lower measured Q-factor of 2200 ± 200, which is less than the $\sim$20 000 estimated from simulation and it is likely that this is due to fabrication imperfections. It is thought that the 200-GHz

TABLE II
Q-FACTOR AND MODAL VOLUME OF RESONANT MODES

Resonance No.	Measured Q-factor		Eff. Modal Vol. (mm^3)	
	100-GHz	200-GHz	100-GHz	200-GHz
1	$11\,900 \pm 500$	2200 ± 200	0.28	0.077
2	6800 ± 300	660 ± 40	0.43	0.11
3	2600 ± 100	270 ± 20	0.53	0.15
4	610 ± 30	200 ± 10	0.64	0.17

device is more sensitive to this than the 100-GHz device, due to the larger hole radii relative to the microbeam width which creates narrow silicon regions around the holes (see Fig. 4). The large hole size was necessary to open a bandgap at the higher frequency and this limitation may be alleviated in future devices by using a thinner silicon wafer. It can also be seen in Table II that the Q-factor of the higher order modes decreases with mode order, due to increased waveguide loss, since the larger modal volume couples more strongly with the DRW mode.

The surface roughness and vertical profile of etched sidewalls produced by the employed DRIE process have been analyzed in [23] and found to produce surfaces with low roughness and a mean "scalloping" of 8 nm in high aspect ratio channels. The process was also shown to be more dependent on the aspect ratio of the structures to be etched than the feature size, meaning that devices operating at higher resonant frequencies should be possible if the thickness of the silicon wafer is reduced to maintain the aspect ratio of the features. The DRIE minimum feature size is primarily limited by the optical lithography which can be submicron, depending upon the light source. The main barrier to scaling the devices to higher frequencies is likely to be the inherent fragility of the devices due to the thinness of the silicon wafer required for higher frequency operation. For a silicon wafer with a thickness of 100 μm, it may be possible to reach $\sim$1 THz; however, further increases in frequency will likely require the silicon to be mechanically supported by a carrier substrate. This approach has been successfully demonstrated in the IR and optical regimes where a common fabrication technique is to use RIE of the silicon layer of an SOI wafer to create the nanobeam resonators [8]–[15].

B. Resonance Modal Volumes

The effective mode volume for the resonant mode of a PCR is commonly calculated using the following expression [6]:

$$V = \frac{\int_v \epsilon |E|^2 \, dV}{\left[\epsilon |E|^2 \right]_{\max}}. \qquad (5)$$

From electromagnetic simulations, the modal volume of the fundamental mode is calculated to be 0.28 mm^3 ($= 0.51 \, (\lambda / \sqrt{\epsilon'_r})^3$) and 0.077 mm^3 ($= 0.83 \, (\lambda / \sqrt{\epsilon'_r})^3$) for the 100- and 200-GHz devices, respectively. It should be noted that (5) tends to underestimate the physical modal volume, due to the high peak electric field intensity in the center of the cavity,

making the denominator large. Table II summarizes the effective modal volume for all the resonances.

The resonators were not optimized for a small modal volume and this could be made smaller by reducing N; despite this, the calculated volumes compare favorably with the *L*3 (0.73 $(\lambda/\sqrt{\epsilon'_r})^3$ [27]) and heterostructure (1.2 $(\lambda/\sqrt{\epsilon'_r})^3$ [28]) 2-D photonic crystal slab resonators demonstrated within the IR region. This small volume allows high Purcell factors $\propto (Q/V)(\lambda/\sqrt{\epsilon'_r})^3$. However, the lower *Q*-factor limits the Purcell factor when compared to other regions of the electromagnetic spectrum [16], [18].

The small resonant mode volume of the resonators makes them ideally suited for the integration on a silicon substrate, alongside other waveguide structures and components. In the future, drop-out filters, diplexers [29], switches [30], and waveguide couplers could be constructed by bringing-in a second suspended silicon DRW, in close proximity to the microbeam, to create coupling between the two.

V. PHOTOCONDUCTIVE TUNING OF THE RESONANCE

The MPCRs display a strong sensitivity to light, due to above-bandgap energy photons generating photo-induced carriers within the silicon, increasing its conductivity and damping the *Q*-factor of the resonance. This sensitivity is sufficiently high that ripple is evident in S_{21} frequency responses under standard laboratory light-emitting diode (LED) lighting due to light flicker.

The complex permittivity of silicon can be expressed as

$$\epsilon = \epsilon_0 \left(\epsilon'_r - j\frac{\sigma}{\omega\epsilon_o} \right) \tag{6}$$

where σ is the conductivity due to free carriers, ω the angular frequency, and ϵ_o is the permittivity of free-space. Here, it is assumed that at the frequencies of interest, the imaginary component of the permittivity is dominated by the free-carrier conductivity [31]. Combining (3) and (6), the *Q*-factor of the resonator in the material loss-limited regime can be expressed as

$$Q_l \approx \frac{\omega\epsilon_o\epsilon'_r}{\sigma\rho}. \tag{7}$$

From this, it can be observed that the *Q*-factor will be strongly influenced by the silicon conductivity when operating in this regime. The conductivity of the silicon is proportional to the density of free-carriers and this underscores the need for the device to be fabricated from HRS to achieve a high *Q*-factor. This sensitivity to free-carriers can be exploited to tune a resonance of the MPCR using photo-illumination.

For our study, the 100-GHz MPCR was used, as it was found to be more sensitive than the 200-GHz device, attributed to the device's higher *Q*-factor and electric field filling factor (0.92 versus 0.77). To investigate the light sensitivity, the output of a high-intensity LED was focused onto one side of the microbeam (normal incidence in the *X–Y* plane) using two planoconvex lenses. The beam was slightly defocused to maximize the attenuation of the resonance, which corresponded to a spot size of ∼9 mm centered on the middle of the microbeam.
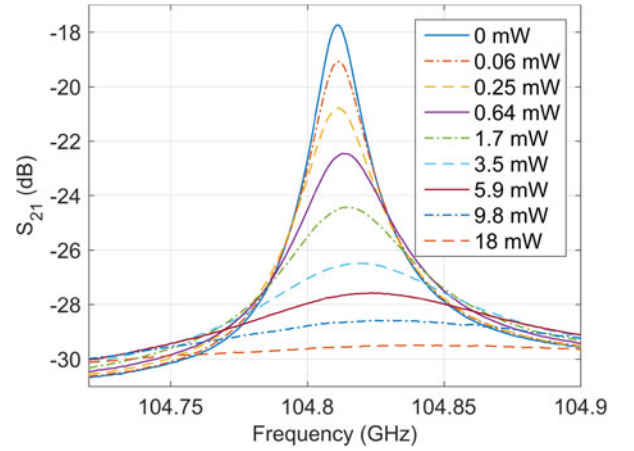

Fig. 9. Modulation of the second resonance of the 100-GHz MPCR using photoconductive tuning by an IR LED at 910 ± 10 nm.

Examining the absorption coefficient of intrinsic silicon [32] for visible and IR radiation indicates that a wavelength of 1.04 μm corresponds to an absorption length that is approximately equal to the microbeam thickness. However, it was found empirically that an LED (Thorlabs LED910E) with a center wavelength of 910 ± 10 nm, which has a shorter absorption length, results in a stronger response. Fig. 9 shows the variation in the measured S_{21} of the second resonance with optical output power from this LED.

The second resonance was chosen due to its balance between *Q*-factor and amplitude, but similar results were observed at other resonances. It can be seen from Fig. 9 that increasing the power of optical illumination reduces the *Q*-factor of the resonance, with only a slight frequency perturbation of the resonance frequency. Furthermore, only a small amount of optical power is required to completely extinguish the resonance. This occurred at 18 mW, but it is estimated geometrically that only 20% of this light was incident upon the microbeam and, hence, only a small fraction of this power would be required in a properly focused system. This result compares favorably with our previous work [33], where we optically modulated a defect waveguide in a 2-D silicon photonic crystal slab operating at similar frequencies— showing that greater illuminating optical powers are required to attenuate a signal to the same level. The improvement in efficiency is attributed to the resonant nature of the transmission response; however, this comes at the expense of narrowband operation.

Green and red LEDs with center wavelengths of 505 and 636 nm, respectively, were also trialed and found to be able to modulate the resonance but with a lower efficiency and to a lesser extent (∼9 dB reduction in peak amplitude). The absorption depth for these wavelengths in silicon is only of the order of several microns [32] and the effectiveness of the modulation at these wavelengths can be explained by the long diffusion length of the photocarriers (∼200 μm) and the high electric field intensities of the resonant modes near to the surface in the silicon, as shown in Fig. 8.
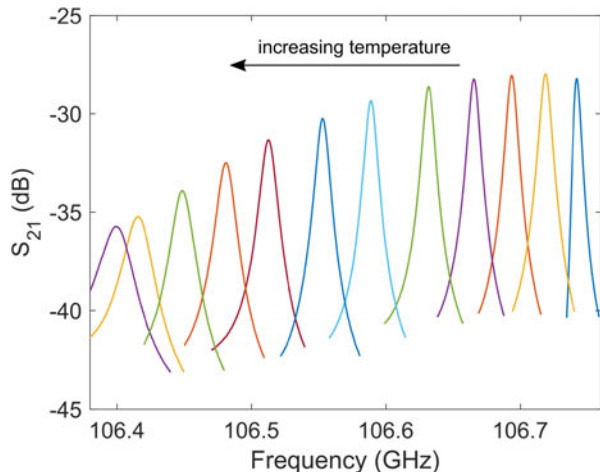
Fig. 10.   Thermal tuning of the fundamental resonance of the 100-GHz MPCR for the temperature range from 295 to 350 K.

VI. THERMAL TUNING OF THE RESONANCE

The temperature-dependent nature of the permittivity of silicon provides another opportunity for tuning the response of the resonator. It also highlights the need for the resonator to be temperature-stabilized, if employed in a terahertz oscillator. Rearranging (6) to include the loss tangent and introducing a temperature T dependency gives

$$\epsilon(T) = \epsilon_0 \epsilon_r'(T)\left(1 - j\tan\delta(T)\right). \tag{8}$$

As a first approximation, the thermal characteristics of the MPCR are assumed to behave similar to a dielectric-filled cavity resonator, where the resonant frequency is inversely proportional to the cavity optical length (i.e., $f_c \propto 1/a\sqrt{\epsilon_r'}$ and assuming $\rho \approx 1$). It follows that the sensitivity of the resonant frequency with temperature can be expressed as [1]

$$\frac{\Delta f_c}{f_c} = -\left(\alpha + \frac{1}{2}\tau_\epsilon\right)\Delta T \tag{9}$$

where α is the thermal expansion coefficient and τ_ϵ the temperature coefficient of the dielectric constant of silicon. Using published data for silicon at room-temperature yields $\tau_\epsilon = \epsilon_r'^{-1} d\epsilon_r'/dT = 1.1 \times 10^{-4}$ K^{-1} [34] and $\alpha = 2.6 \times 10^{-6}$ K^{-1} [35], which lead to a temperature coefficient for the resonant frequency of 58 ppm/°C. To test this, a hot air gun was used to warm up the silicon of the 100-GHz MPCR. Fig. 10 shows the variation in S_{21} for the fundamental resonant mode as the air temperature is increased from approximately 295 to 350 K. The observed frequency change across the temperature range is within a few percent of that predicted by (9).

The behavior of the loss tangent of silicon as a function of temperature is more complicated than for the real part of permittivity. For temperatures above $\sim$310 K, the silicon becomes intrinsic and the loss tangent increases rapidly with temperature, due to thermally induced carrier generation [34], limiting the useable tuning range. This can be observed in Fig. 10,

where the resonance can be seen to broaden with increasing temperature.

Below room-temperature, the loss tangent increases with decreasing temperature until very low temperatures are reached due to the increase in carrier mobility and, consequently, conductivity [34]. This increase in loss tangent occurs more slowly than for heating above room-temperature and therefore, cooling the MPCR may offer a better route to tuning.

With respect to temperature stabilization, preliminary simulations have shown that the microbeam temperature can be readily controlled through the placement of a microheater (e.g., resistive or Peltier) on one or both of the support mounts and the high thermal conductivity of silicon can be utilized to transfer the heat across the supporting beams to the microbeam.

In addition to tuning an oscillator, the ability to vary the resonant frequency or Q-factor of an MPCR opens up opportunities for new switching devices, where coupling between several adjacent resonant cavities is controlled by on-chip microheaters or LEDs (see for example [36]).

VII. CONCLUSION

The design of high Q-factor terahertz resonators through the engineering of 1-D bandgaps in suspended HRS DRW was demonstrated. The approach was validated through the fabrication of two MPCRs operating at 100- and 200-GHz, with respective measured Q-factors of 11 900 and 2200 with their fundamental modes.

Both phototuning and thermal-tuning of the MPCRs were investigated. The 100-GHz MPCR was found to be extremely sensitive to light, which allowed the resonance Q-factor to be tuned and even extinguished altogether through illumination with a single IR LED. Additionally, thermal tuning was shown to offer limited tuning of the resonance frequency. A simple approach to packaging the device in a low-cost 3-D-printed housing, which interfaces well to precision metal-pipe rectangular waveguide flanges, was also shown.

This work allows for the creation of low-loss waveguide, resonators, impedance matching, and filtering from suspended DRW, while also laying the foundations for microphotonic-integrated circuits with terahertz systems-on-a-substrate technologies.

REFERENCES

[1] D. Kajfez and P. Guillon, *Dielectric Resonators*, 2nd ed. New York, NY, USA: Noble, 1986.

[2] S. M. Hanham, C. Watts, W. J. Otter, S. Lucyszyn, and N. Klein, "Dielectric measurements of nanoliter liquids with a photonic crystal resonator at terahertz frequencies," *Appl. Phys. Lett.*, vol. 107, no. 3, Jul. 2015, Art. no. 32903.

[3] E. N. Shaforost, N. Klein, S. A. Vitusevich, A. Offenhäusser, and A. A. Barannik, "Nanoliter liquid characterization by open whispering-gallery mode dielectric resonators at millimeter wave frequencies," *J. Appl. Phys.*, vol. 104, 2008, Art. no. 74111.

[4] A. Malekabadi, S. A. Charlebois, D. Deslandes, and F. Boone, "High-resistivity silicon dielectric ribbon waveguide for single-mode low-loss propagation at F/G-bands," *IEEE Trans. THz Sci. Technol.*, vol. 4, no. 4, pp. 447–453, Jul. 2014.

[5] N. Ranjkesh, M. Basha, A. Taeb, and S. Safavi-Naeini, "Silicon-on-glass dielectric waveguide—Part II: For THz applications," *IEEE Trans. THz Sci. Technol.*, vol. 5, no. 2, pp. 280–287, Mar. 2015.

[6] J. D. Joannopoulos, S. G. Johnson, J. N. Winn, and R. D. Meade, *Photonic Crystals: Molding the Flow of Light*, 2nd ed. Princeton, NJ, USA: Princeton Univ., 2011.

[7] S. Fan *et al.*, "Guided and defect modes in periodic dielectric waveguides," *J. Opt. Soc. Amer. B*, vol. 12, no. 7, pp. 1267–1272, Jul. 1995.

[8] J. S. Foresi *et al.*, "Photonic-bandgap microcavities in optical waveguides," *Nature*, vol. 390, no. 6656, pp. 143–145, Nov. 1997.

[9] M. Miri *et al.*, "Design and fabrication of photonic crystal nano-beam resonator: Transmission line model," *J. Lightw. Technol.*, vol. 32, no. 1, pp. 91–98, Jan. 2014.

[10] A. R. Md Zain, N. P. Johnson, M. Sorel, and R. M. De La Rue, "Ultra high quality factor one dimensional photonic crystal/photonic wire micro-cavities in silicon-on-insulator (SOI)," *Opt. Exp.*, vol. 16, no. 16, pp. 12084–12089, Aug. 2008.

[11] P. B. Deotare, M. W. McCutcheon, I. W. Frank, M. Khan, and M. Lonččar, "High quality factor photonic crystal nanobeam cavities," *Appl. Phys. Lett.*, vol. 94, no. 12, Mar. 2009, Art. no. 121106.

[12] P. Seidler, K. Lister, U. Drechsler, J. Hofrichter, and T. Stöferle, "Slotted photonic crystal nanobeam cavity with an ultrahigh quality factor-to-mode volume ratio," *Opt. Exp.*, vol. 21, no. 26, pp. 32468–32483, Dec. 2013.

[13] J. D. Ryckman and S. M. Weiss, "Low mode volume slotted photonic crystal single nanobeam cavity," *Appl. Phys. Lett.*, vol. 101, no. 7, Aug. 2012, Art. no. 71104.

[14] M. W. McCutcheon, P. B. Deotare, Y. Zhang, and M. Lonččar, "High-Q transverse-electric/transverse-magnetic photonic crystal nanobeam cavities," *Appl. Phys. Lett.*, vol. 98, no. 11, 2011, Art. no. 111117.

[15] Q. Quan and M. Loncar, "Deterministic design of wavelength scale, ultrahigh Q photonic crystal nanobeam cavities," *Opt. Exp.*, vol. 19, no. 19, pp. 18529–18542, Sep. 2011.

[16] Y. Zhang *et al.*, "High-Q/V air-mode photonic crystal cavities at microwave frequencies," *Opt. Exp.*, vol. 19, no. 10, pp. 9371–9377, May 2011.

[17] E. M. Purcell, "Spontaneous emission probabilities at radio frequencies," *Phys. Rev.*, vol. 69, p. 681, 1946.

[18] S. Noda, M. Fujita, and T. Asano, "Spontaneous-emission control by photonic crystals and nanocavities," *Nature Photon.*, vol. 1, no. 8, pp. 449–458, Aug. 2007.

[19] Y. Akahane, T. Asano, B. S. Song, and S. Noda, "High-Q photonic nanocavity in a two-dimensional photonic crystal," *Nature*, vol. 425, no. 6961, pp. 944–947, 2003.

[20] Q. Quan, P. B. Deotare, and M. Loncar, "Photonic crystal nanobeam cavity strongly coupled to the feeding waveguide," *Appl. Phys. Lett.*, vol. 96, no. 20, 2010, Art. no. 203102.

[21] S. G. Johnson and J. D. Joannopoulos, "Block-iterative frequency-domain methods for Maxwell's equations in a planewave basis," *Opt. Exp.*, vol. 8, no. 3, pp. 173–190, 2001.

[22] S. Lucyszyn, Ed., *Advanced RF MEMS*. Cambridge, U.K.: Cambridge Univ., 2010.

[23] W. T. Pike, W. J. Karl, S. Kumar, S. Vijendran, and T. Semple, "Analysis of sidewall quality in through-wafer deep reactive-ion etching," *Microelectron. Eng.*, vol. 73–74, pp. 340–345, Jun. 2004.

[24] W. J. Otter *et al.*, "100 GHz ultra-high Q-factor photonic crystal resonators," *Sens. Actuators A*, vol. 217, pp. 151–159, 2014.

[25] J. W. Lamb, "Miscellaneous data on materials for millimetre and submillimetre optics," *Int. J. Infrared Millim. Waves*, vol. 17, no. 12, pp. 1997–2034, 1996.

[26] D. Kajfez, S. Chebolu, M. R. Abdul-Gaffoor, and A. A. Kishk, "Uncertainty analysis of the transmission-type measurement of Q-factor," *IEEE Trans. Microw. Theory Techn.*, vol. 47, no. 3, pp. 367–371, Mar. 1999.

[27] T. Asano, B.-S. Song, Y. Akahane, and S. Noda, "Ultrahigh-Q nanocavities in two-dimensional photonic crystal slabs," *IEEE J. Sel. Top. Quantum Electron.*, vol. 12, no. 6, pp. 1123–1134, Nov. 2006.

[28] Y. Tanaka, T. Asano, and S. Noda, "Design of photonic crystal nanocavity with Q-factor of ~10ˆ9," *J. Lightw. Technol.*, vol. 26, no. 11, pp. 1532–1539, Jun. 2008.

[29] M. Yata, M. Fujita, and T. Nagatsuma, "Photonic-crystal diplexers for terahertz-wave applications," *Opt. Exp.*, vol. 24, no. 7, pp. 7835–7849, Apr. 2016.

[30] V. Dmitriev and L. Martins, "Two-dimensional photonic-crystal-based double switch-divider," *Appl. Opt.*, vol. 55, no. 13, pp. 3676–3680, May 2016.

[31] V. V. Parshin, R. Heidinger, B. A. Andreev, A. V. Gusev, and V. B. Shmagin, "Silicon as an advanced window material for high power gyrotrons," *Int. J. Infrared Millim. Waves*, vol. 16, no. 5, pp. 863–877, May 1995.

[32] M. A. Green, "Self-consistent optical parameters of intrinsic silicon at 300K including temperature coefficients," *Sol. Energy Mater. Sol. Cells*, vol. 92, no. 11, pp. 1305–1310, 2008.

[33] W. J. Otter, S. M. Hanham, N. Klein, S. Lucyszyn, and A. S. Holmes, "W-band laser-controlled photonic crystal variable attenuator," in *Proc. IEEE Int. Microw. Symp.*, 2014, pp. 1–3.

[34] J. Krupka *et al.*, "Measurements of permittivity, dielectric loss tangent, and resistivity of float-zone silicon at microwave frequencies," *IEEE Trans. Microw. Theory Techn.*, vol. 54, no. 11, pp. 3995–4001, Nov. 2006.

[35] C. A. Swenson, "Recommended values for the thermal expansivity of silicon from 0 to 1000 K," *J. Phys. Chem. Ref. Data*, vol. 12, no. 2, pp. 179–182, 1983.

[36] R. Konoike *et al.*, "On-demand transfer of trapped photons on a chip," *Sci. Adv.*, vol. 2, no. 5, 2016, Art. no. e1501690.

Stephen M. Hanham (S'03–M'10) received the B.E. degree in electronic engineering and B.Sc. degree in computer science from the University of Western Australia, Perth, Australia, in 2004, and the Ph.D. degree in electronic engineering from the University of Sydney, Sydney, Australia, in 2010.

From 2008 to 2010, he was a Research Project Officer and later a Systems Engineer with the Commonwealth Scientific and Industrial Research Organization, Sydney, Australia, working on THz antennas and detectors, mobile satellite terminals, and radio telescope antenna systems. Currently, he is working at Imperial College London, London, U.K., as a Research Associate in the area of near-field terahertz imaging and sensing, spectroscopy, and plasmonics. His research interests include electromagnetics, plasmonics, nanomaterials, antennas, and terahertz and microwave technologies.

Munir M. Ahmad received the Ph.D. degree in chemistry on the synthesis, electrical, and magnetic properties of organic semiconductors from the University of Bradford, Bradford, U.K., in 1978.

He has worked on the design, synthesis, and application of electroactive and specialty polymers. He joined the Optical and Semiconductor Devices Group, Department of Electrical and Electronic Engineering, Imperial College London, London. U.K., in 1993 and has worked on a number of projects related to microengineering, microelectromechanical systems, and materials for optical devices.

Dr. Ahmad is a Chartered Chemist and a Fellow of the Royal Society of Chemistry.

Stepan Lucyszyn (M'91–SM'04–F'14) received the Ph.D. degree in electronic engineering from the King's College London (University of London), London, U.K., in 1992, and the D.Sc. degree in millimeter-wave and terahertz electronics from the Imperial College London, London, U.K., in 2010.

After working in industry as a Satellite Systems Engineer for maritime and military communications, he went into academia. He is a Professor of millimetre-wave systems and the Director of the Centre for Terahertz Science and Engineering, Imperial College London, London, U.K. He has co-authored approximately 180 papers and 12 book chapters in applied physics and electronic engineering. He co-founded the Imperial College London spin-out company Drayson Wireless Ltd., Apr. 2014.

Dr. Lucyszyn was appointed an IEEE Distinguished Microwave Lecturer (DML) (2010–2012) and Emeritus DML (2013). In 2011, he was the Chairman of the 41st European Microwave Conference, Manchester, U.K. He is currently a European Microwave Lecturer for the European Microwave Association.

Norbert Klein received the diploma and Ph.D. degree in physics from the University of Wuppertal, Wuppertal, Germany, in 1985 and 1989, respectively, and the "Habilitation" degree in physics from the Technical University of Aachen, Aachen, Germany, in 1998.

He is a Full Professor and the Chair in electromagnetic materials with the Imperial College London, London, U.K., and the Director of the Imperial's Centre of Terahertz Science and Engineering. Before 2009, he was the Division Leader for electromagnetic sensors with the Julich Research Center, Julich, Germany, and was lecturing at Technical Universities of Aachen and Dortmund in Germany. He is the (co)author of more than 172 peer-reviewed scientific papers and book articles with a h-index of 27 and is a key inventor on more than 10 European and U.S. patents related to microwave devices for sensor and communication applications. In 2007, he founded a spin-off company which has successfully commercialized a microwave sensor system for airport security. His current research interests include microwave and terahertz sensors for biomedical and security applications and low-dimensional nanomaterials for high-frequency applications.